A Fixed Switching Frequency Direct Model Predictive Control for Neutral-Point-Clamped Three-Level Inverters with Induction Machines

Qifan Yang, *Student Member, IEEE*, Petros Karamanakos, *Senior Member, IEEE*,
Eyke Liegmann, *Student Member, IEEE*, Wei Tian, *Student Member, IEEE*, Tobias Geyer, *Fellow, IEEE*,
Ralph Kennel, *Senior Member, IEEE*, and Marcelo Lobo Heldwein, *Senior Member, IEEE*

Abstract—This article presents a direct model predictive control (MPC) scheme for drive systems consisting of a three-phase three-level neutral-point-clamped (3L-NPC) inverter and an induction machine (IM). Even though the discussed MPC algorithm is a direct control strategy, it operates the inverter at a fixed switching frequency, while the output harmonic spectrum of the stator current is discrete, with harmonics at non-triplen, odd integer multiples of the fundamental frequency. As a result, the proposed method achieves similar or superior steady-state behavior than that of modulator-based control schemes. Moreover, thanks to its direct control nature, it exhibits the fast transient responses that characterize direct controllers due to the absence of an explicit modulator. Furthermore, the multiple control objectives of the system, i.e., stator current control and neutral point (NP) potential balancing, are addressed in one computational stage, thus avoiding any additional control loops in a cascaded or parallel structure. This favorable control structure is facilitated by the adopted modeling approach, according to which the system behavior is described by the gradient of the system output. In doing so, not only a simple, versatile system model is derived, but also the direct MPC can be formulated as a constrained quadratic program (QP), which can be easily solved in real time with an in-house solver. The effectiveness of the proposed control scheme is experimentally verified on a 4-kW drive system.

Index Terms—AC drives, model predictive control (MPC), direct control, multiple-input multiple-output (MIMO) systems, power electronic systems, three-level neutral point clamped (NPC) inverters.

I. Introduction

THE three-level neutral-point-clamped (3L-NPC) inverter [1] has been widely used in high-power medium-voltage (MV) applications, such as MV motor drives [2], wind power generations [3], and electric vehicle charging stations [4]. Compared to the traditional two-level converters, the NPC converters can reduce the harmonics of the output voltage and current, and they are more suitable for higher voltage and power applications since the voltage stress is distributed over the series-connected power devices. However, the multilevel output and the floating neutral point (NP) make the modulation and control design more complex.

To address the latter challenge, several studies have focused on the NP potential balancing problem. As shown in [5], the NP potential can be balanced by manipulating the common-mode voltage (CMV). As a result, the modulating signal that is fed into a carrier-based pulse width modulator (CB-PWM) can be injected with a suitable CMV signal to achieve balancing of the NP potential. This signal, e.g., can be derived from a simple closed-loop NP potential controller based on a proportional-integral (PI) controller [6]. However, this control loop becomes unstable when the power factor (PF) approaches zero. For this reason, the NP potential control loop needs to be disabled when working in this operating region.

Based on the same principle, the NP potential control in space vector modulation (SVM) is achieved by manipulating the ratio of the redundant voltage vectors, which essentially is equivalent to adjusting the CMV [7]. In this direction, [8] proposed an SVM method which can effectively balance the NP potential over a wide range of modulation indices as well as at zero PF conditions. However, to do so, the inverter occasionally operates in bipolar mode, which not only is considerably complicated to implement, but also results in an increased switching frequency.

An alternative approach that has shown to be particularly effective with such challenging problems as the discussed one is direct model predictive control (MPC) with reference tracking, also known as finite control set MPC (FCS-MPC). This is thanks to its ability to tackle several control objectives in one computational stage by solving a multicriterion optimization in real time [9]. Indeed, an FCS-MPC scheme for a 3L-NPC was first presented in [10]. Albeit its simple structure, the presented FCS-MPC algorithm successfully controls the load current and NP potential at both steady-state and transient operation. However, the ℓ_1-norm in the objective function and the single-step prediction horizon lead to deteriorated control performance as well as potential closed-loop stability issues, especially when operating at low switching frequencies [11]. To improve the performance of FCS-MPC, it is favorable to use the ℓ_2-norm in the objective function [12], longer prediction horizons [13], [14] and shorter sampling intervals [11], which, however, pose a big computational challenge for a real-time implementation [15]. Besides, the direct control nature of

Q. Yang, E, Liegmann, W. Tian, R. Kennel and M. L. Heldwein are with the Chair of High-Power Converter Systems, Technical University of Munich, 80333 Munich, Germany; e-mail: qifan.yang@tum.de, eyke.liegmann@tum.de, wei.tian@tum.de, raphel.kennel@tum.de, marcelo.heldwein@tum.de

P. Karamanakos is with the Faculty of Information Technology and Communication Sciences, Tampere University, 33101 Tampere, Finland; e-mail: p.karamanakos@ieee.org

T. Geyer is with ABB Systems Drives, 5300 Turgi, Switzerland; e-mail: t.geyer@ieee.org

the method, i.e., the controller directly generates the switching signals without requiring a dedicated modulation stage, gives rise to a variable switching frequency and a spread current harmonic spectrum as well as nondeterministic power losses and unequal distribution of the load, which can be undesirable in many applications [16], [17].

To address the above-mentioned drawbacks of FCS-MPC, some direct MPC algorithms with an implicit modulator for NPC converters have been proposed [18]–[20]. The method in [18] adopts the concept of optimal switching sequences (OSSs) [21], according to which the candidate switching patterns imitate those of CB-PWM/SVM. In a subsequent step, the optimal one is selected by solving an optimization problem, and it is applied at the corresponding optimal switching time instants. In doing so, a fixed switching frequency and concentrated current harmonic spectra are achieved. However, the optimization problem that computes the optimal switching times is formulated as an unconstrained quadratic program (QP), meaning that it might yield a solution that violates the physical limits of the converter, e.g., a switching time instant that is negative or larger than the sampling interval. In such a case, a simple saturation strategy is normally used, which, alas, does not always guarantee optimality. To address this, the OSS-based methods in [19] and [20], introduce constraints to the optimization problem formulation. However, the design of the objective functions does not ensure zero—or even small—reference tracking error at the discrete time instants at steady-state operation, while it does not directly account for the ripple of the controlled variables. As a result, when sampling occurs, the ripple of the current enters the inner control loop, thus leading to undesired low-frequency harmonics, and increased overall harmonic distortions [22]. Moreover, the adopted cascaded structures lead to uncoordinated control/modulation, and thus the multi-objective control feature of MPC as well as the benefits of direct control are not fully exploited [23]. Hence, as not all features of direct MPC are utilized to the fullest extent possible, the most favorable steady-state and/or dynamic system behavior is not ensured.

To tackle the aforementioned issues, a direct MPC method with an implicit modulator for variable speed drive systems was proposed in [24]. This method uses the gradient of the system output to predict the future behavior of the drive. In doing so, not only a simple and versatile—yet sufficiently accurate—modeling approach is employed, but also the formulation of the optimal control problem as a constrained QP is enabled. As a result, its real-time implementation is greatly facilitated [25] as well as its extension to different power electronic systems [22]. Furthermore, the objective function is formulated such that a fixed switching frequency is ensured along with zero current ripple at the discrete time instants. As a result, low current distortions are produced with the harmonic power being concentrated at frequencies which are at odd, non-triplen integer multiples of the fundamental.

This article employs the above-mentioned direct MPC scheme to control a three-phase 3L-NPC inverter driving an induction machine (IM). Besides the control of the stator current, the developed control algorithm successfully and effectively balances the NP potential, even under challenging
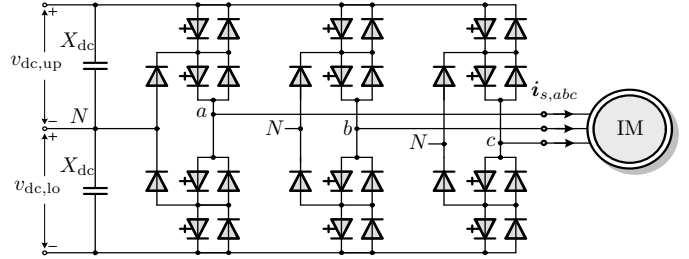

Fig. 1: Three-level three-phase neutral point clamped (NPC) voltage source inverter driving an induction motor (IM).

operating conditions, such as at zero PF. To achieve this, the NP potential balancing is addressed in the same computational stage with the stator current control problem to allow for coordinated—and thus more effective—control. In doing so, a very simple control structure results, thus demonstrating the high versatility of the developed algorithm along with its ability to handle multiple-input and multiple-output (MIMO) systems with complex and nonlinear dynamics. Moreover, to facilitate the real-time implementation of the proposed direct MPC strategy, the deadbeat solution is employed to reduce the number of candidate switching sequences. As a result, the maximum number of candidate solutions remains relatively low and independent of the voltage levels of the converter. Therefore, this solution enables the extension of the proposed direct MPC method to multilevel converters with no additional computational overhead. Furthermore, to further alleviate the computational load of the proposed MPC method, the QP algorithm developed in [25] is refined and tailored to the specific optimization problem at hand. Finally, owing to the direct control principle of the developed method, fast transients are achieved, limited only by the available dc-link voltage. This advantageous steady-state and dynamic performance of the proposed method is experimentally verified and highlighted by benchmarking it against conventional field oriented control (FOC) with SVM.

This paper is structured as follows. Section II introduces the mathematical model of the drive system that serves as a case study. The direct MPC scheme is presented in Section III, and its performance is experimentally evaluated and compared with three conventional control methods in Section IV. Finally, Section V concludes the paper.

II. MATHEMATICAL MODEL OF THE SYSTEM

In this work, the modeling of the system is done in the stationary orthogonal $\alpha\beta$ reference frame. To this end, any variable $\boldsymbol{\xi}_{abc} = [\xi_a\ \xi_b\ \xi_c]^T$ in the abc-plane is mapped into a variable $\boldsymbol{\xi}_{\alpha\beta} = [\xi_\alpha\ \xi_\beta]^T$ in the $\alpha\beta$-plane via $\boldsymbol{\xi}_{\alpha\beta} = \boldsymbol{K}\boldsymbol{\xi}_{abc}$,[1] where

$$\boldsymbol{K} = \frac{2}{3} \begin{bmatrix} 1 & -\frac{1}{2} & -\frac{1}{2} \\ 0 & \frac{\sqrt{3}}{2} & -\frac{\sqrt{3}}{2} \end{bmatrix} . \qquad (1)$$

Moreover, throughout this paper, all quantities are normalized and presented in the per unit (p.u.) system.

---

[1]In the sequel of the paper, the subscript $\alpha\beta$ used to denote variables in the $\alpha\beta$-plane is omitted to simplify the notation. Variables in the abc-plane are indicated with the corresponding subscript.

Fig. 1 shows the structure of a 3L-NPC voltage source inverter driving an IM. The 3L-NPC is connected to a stiff dc voltage supply and the NP is floating. Thus, the total dc-link voltage is constant and it is given by $v_{dc} = v_{dc,up} + v_{dc,lo}$, where $v_{dc,up}$ and $v_{dc,lo}$ denote the voltage over the upper and lower dc-link capacitors, respectively.

Let $\boldsymbol{u}_{abc} = [u_a \ u_b \ u_c]^T$ denote the three-phase switch position of the 3L-NPC, where $u_x \in \mathcal{U} = \{-1, 0, 1\}$, with $x \in \{a, b, c\}$, is the single-phase switch position. In each phase, the values $-1, 0$, and 1 correspond to the phase voltages $-v_{dc,lo}, 0$, and $v_{dc,up}$, respectively. Thus, the output voltage of the inverter $\boldsymbol{v}_{inv}$—which is equal to the stator voltage $\boldsymbol{v}_s$—is

$$\boldsymbol{v}_{inv} = \boldsymbol{v}_s = \frac{v_{dc}}{2}\boldsymbol{K}\boldsymbol{u}_{abc} - v_n\boldsymbol{K}|\boldsymbol{u}_{abc}|, \qquad (2)$$

where $|\boldsymbol{u}_{abc}| = [|u_a| \ |u_b| \ |u_c|]^T$ is the component-wise absolute value of $\boldsymbol{u}_{abc}$. In (2), v_n stands for the NP potential given by

$$v_n = \frac{1}{2}(v_{dc,lo} - v_{dc,up}), \qquad (3)$$

and it evolves according to

$$\frac{dv_n}{dt} = \frac{1}{2X_{dc}}|\boldsymbol{u}_{abc}|^T\boldsymbol{i}_{abc}, \qquad (4)$$

where X_{dc} is the (inverse) reactance of the dc-link capacitor.

The dynamics of the IM can be described by choosing the stator current $\boldsymbol{i}_s$ and the rotor flux $\boldsymbol{\psi}_r$ as the state of the machine, i.e., [26][2]

$$\frac{d\boldsymbol{i}_s}{dt} = -\frac{1}{\tau_s}\boldsymbol{i}_s + \left(\frac{1}{\tau_r}\boldsymbol{I}_2 - \omega_r\begin{bmatrix}0 & -1 \\ 1 & 0\end{bmatrix}\right)\frac{X_m}{D}\boldsymbol{\psi}_r + \frac{X_r}{D}\boldsymbol{v}_s \qquad (5a)$$

$$\frac{d\boldsymbol{\psi}_r}{dt} = \frac{X_m}{\tau_r}\boldsymbol{i}_s - \frac{1}{\tau_r}\boldsymbol{\psi}_r + \omega_r\begin{bmatrix}0 & -1 \\ 1 & 0\end{bmatrix}\boldsymbol{\psi}_r, \qquad (5b)$$

where R_s (R_r) is the stator (rotor) resistance, X_{ls} (X_{rs}) the stator (rotor) leakage reactance, and X_m the mutual reactance. Moreover, $\tau_s = X_r D / (R_s X_r^2 + R_r X_m^2)$ is the transient stator time constant and $\tau_r = X_r / R_r$ the rotor time constant, where the constant D is defined as $D = X_s X_r - X_m^2$, with $X_s = X_{ls} + X_m$ and $X_r = X_{lr} + X_m$.

The system of equations (5) can be written in the following compact continuous-time state-space form

$$\frac{d\boldsymbol{x}_m(t)}{dt} = \boldsymbol{F}_m\boldsymbol{x}_m(t) + \boldsymbol{G}_m\boldsymbol{v}_s(t) \qquad (6a)$$

$$\boldsymbol{y}_m(t) = \boldsymbol{C}_m\boldsymbol{x}_m(t), \qquad (6b)$$

where $\boldsymbol{x}_m = [i_{s\alpha} \ i_{s\beta} \ \psi_{r\alpha} \ \psi_{r\beta}]^T$ and $\boldsymbol{y}_m = [i_{s\alpha} \ i_{s\beta}]^T$. Combining (6) with (4) and (2) yields that state-space representation of the drive system, i.e.,

$$\frac{d\boldsymbol{x}(t)}{dt} = \boldsymbol{F}(\boldsymbol{u}_{abc}(t))\boldsymbol{x}(t) + \boldsymbol{G}\boldsymbol{u}_{abc}(t) \qquad (7a)$$

$$\boldsymbol{y}(t) = \boldsymbol{C}\boldsymbol{x}(t), \qquad (7b)$$

where the state vector is $\boldsymbol{x} = [\boldsymbol{x}_m^T \ v_n]^T$, the three-phase switch position $\boldsymbol{u}_{abc}$ is the system input, and the system

output consists of the stator current and the NP potential, i.e., $\boldsymbol{y} = [\boldsymbol{y}_m^T \ v_n]^T$. Note that the system matrix $\boldsymbol{F}(\boldsymbol{u}_{abc}(t))$, the input matrix $\boldsymbol{G}$, and the output matrix $\boldsymbol{C}$ are provided in the appendix.

Finally, by using forward Euler discretization,[3] the discrete-time state-space model of the system is derived as

$$\boldsymbol{x}(k+1) = \boldsymbol{A}\boldsymbol{x}(k) + \boldsymbol{B}\boldsymbol{u}_{abc}(k) \qquad (8a)$$

$$\boldsymbol{y}(k) = \boldsymbol{C}\boldsymbol{x}(k), \qquad (8b)$$

with $k \in \mathbb{N}$, $\boldsymbol{A} = \boldsymbol{I} + \boldsymbol{F}(\boldsymbol{u}_{abc}(t))T_s$, and $\boldsymbol{B} = \boldsymbol{G}T_s$, where $\boldsymbol{I}$ is the identity matrix of appropriate dimensions, and T_s the sampling interval.

III. DIRECT MPC WITH FIXED SWITCHING FREQUENCY FOR 3L-NPC CONVERTER

In this work, the method proposed in [22], [24] is refined to control the drive system shown in Fig. 1. More specifically, the NP potential balancing is included in the control problem, and a switching sequence set definition based on a deadbeat solution is introduced to reduce the computational burden.

A. Control Problem

The control objectives are threefold. First, the stator current should be regulated along its reference with as little distortion as possible and as quickly as possible so that short settling times are achieved. Second, the NP potential of the 3L-NPC inverter should be balanced under all operating conditions. Finally, operation at a constant switching frequency is desired such that the losses produced in the inverter are constant.

The first two objectives can be achieved by minimizing the weighted (squared) rms value of the output error. This is captured in the objective function of the form

$$J = \frac{1}{T_s}\int_0^{T_s}(\boldsymbol{y}_{ref}(t) - \boldsymbol{y}(t))^T\boldsymbol{Q}(\boldsymbol{y}_{ref}(t) - \boldsymbol{y}(t))dt$$
$$= \frac{1}{T_s}\int_0^{T_s}\left\|\boldsymbol{y}_{ref}(t) - \boldsymbol{y}(t)\right\|_{\boldsymbol{Q}}^2 dt, \qquad (9)$$

where $\boldsymbol{y}_{ref} = [i_{s\alpha,ref} \ i_{s\beta,ref} \ v_{n,ref}]^T$ is the output reference vector, and $\boldsymbol{Q} \succ 0 \in \mathbb{R}^{3\times3}$ the penalty matrix. Here, the penalty matrix is defined as $\boldsymbol{Q} = \text{diag}(1, 1, \lambda_n)$ with $\lambda_n > 0$ being the weighting factor that adjusts the priority of the NP potential balancing.

To meet the third control objective, each phase leg is forced to switch exactly once per sampling interval T_s. To this aim, the vectors of switching time instants $\boldsymbol{t}$ and switch positions $\boldsymbol{U}$ are introduced as

$$\boldsymbol{t} = [t_1 \ t_2 \ t_3]^T$$
$$\boldsymbol{U} = [\boldsymbol{u}_{abc}^T(t_0) \ \boldsymbol{u}_{abc}^T(t_1) \ \boldsymbol{u}_{abc}^T(t_2) \ \boldsymbol{u}_{abc}^T(t_3)]^T. \qquad (10)$$

where

$$0 \leq t_1 \leq t_2 \leq t_3 \leq T_s. \qquad (11)$$

In (10), $\boldsymbol{u}_{abc}(t_0)$ denotes the three-phase switch position at the beginning of the sampling interval, i.e., $t_0 \equiv 0$. At time

---

[2]Note that due to the slower mechanical dynamics, the angular speed of the rotor ω_r is treated as a (relatively slowly) varying parameter rather as a state variable.

[3]When a higher accuracy is required, e.g., at low sampling frequencies, the exact discretization can be used for the IM state-space model (6), see [23, Section 7.2.3] for more details.

TABLE I: Possible switching sequences for a one-step horizon.

Number of sequence	Phase with the switching transition		
	First	Second	Third
1	a	b	c
2	a	c	b
3	b	a	c
4	b	c	a
5	c	a	b
6	c	b	a

TABLE II: Single-phase switching transitions and initial switch position.

Polarity of $u_{\mathrm{db},x}^*$	Sign of Δu_x	Switching transition for u_x	Initial switch position $u_x(t_0)$
≥ 0	$+$	$0 \to 1$	0
≥ 0	$-$	$1 \to 0$	1
< 0	$+$	$-1 \to 0$	-1
< 0	$-$	$0 \to -1$	0

instant t_1, one of the three phase legs switches by applying the switch position $\boldsymbol{u}_{abc}(t_1)$. Similarly, the switch position changes to $\boldsymbol{u}_{abc}(t_2)$ and $\boldsymbol{u}_{abc}(t_3)$ at switching instants t_2 and t_3, respectively, such that the two other yet inactive phase legs are switched in a sequential manner. Finally, the switch position $\boldsymbol{u}_{abc}(t_3)$ is applied until the end of the sampling interval. Thus, the three switching instants divide one sampling interval into four subintervals $[t_i, t_{i+1})$, with $i \in \{0, 1, 2, 3\}$, during which the switch position $\boldsymbol{u}_{abc}(t_i)$ is applied.[4] Based on the above, it can be understood that the three phases can switch in $3! = 6$ possible chronological orders, as summarized in Table I.

B. Selection of Candidate Switching Sequences

Even though there are only six chronological orders with which the three phases can switch, the possible combinations of switch positions are 48.[5] This implies that an equal number of optimization problems (one for each combination) is required to be solved in real time. Such a task, however, is impossible with the available computational resources. Hence, a method to reduce the possible combinations needs to be adopted. To this end, a strategy to define the feasible switch positions within each T_s as well as the initial switch position is introduced, as explained in the following.

Before assessing the possible switching sequences (see Table I), the initial switch position at each sampling interval i.e., $\boldsymbol{u}_{abc}(t_0)$, needs to be determined. To do so, the type of switching transition, defined as $\Delta\boldsymbol{u}_{abc}(k) = \boldsymbol{u}_{abc}(t_3) - \boldsymbol{u}_{abc}(t_0) \in \{-1, 1\}^3$, needs to be examined.[6] In line with the switching pattern of CB-PWM or SVM, the sign of each single-phase transition $\Delta u_x(k)$, $x \in \{a, b, c\}$, is the same for all three phases in one sampling interval T_s, and it alternates between consecutive T_s. For example, if the sign of $\Delta\boldsymbol{u}_{abc}(k)$ is set to be positive in the first T_s, then it is negative in the next T_s, again positive in the third T_s, and so on.

Following, to unequivocally determine $\boldsymbol{u}_{abc}(t_0)$, the deadbeat solution is employed. This is done by considering *only*

---

[4] Note that $t_0 \equiv 0$ and $t_4 \equiv T_s$ denote the beginning and the end of the sampling interval, respectively.

[5] This corresponds to the case where $\boldsymbol{u}_{abc}(t_0) = [0\ 0\ 0]^T$. In such a case, each single-phase switch position can become either 1 or -1 within one T_s. As a result, there are $2^3 = 8$ switching sequences for a given order with which the phases switch. As there are six different chronological orders for the phases to switch (see Table I), the maximum number of candidate switching sequences is $8 \times 6 = 48$.

[6] Directly switching a phase leg from -1 to 1, or vice versa, is forbidden to avoid a potential shoot-through.

the IM dynamics [27]. In doing so, the deadbeat solution is given by[7]

$$\boldsymbol{v}_{\mathrm{db},abc} = \boldsymbol{K}^{-1}\big((\boldsymbol{C}_m\boldsymbol{B}_m)^{-1}(\boldsymbol{y}_{m,\mathrm{ref}}(k+1) - \boldsymbol{C}_m\boldsymbol{A}_m\boldsymbol{x}_m(k)\big). \tag{12}$$

The sign of each entry of $\boldsymbol{v}_{\mathrm{db},abc}$ determines the feasible switch positions. Hence, the combination of the polarity of $v_{\mathrm{db},x}$ and sign of Δu_x defines the initial switch position in phase x. For example, if $v_{\mathrm{db},x} \geq 0$ the feasible switch positions in phase x are either 0 or 1 as a nonnegative output voltage is required. If $\Delta u_x > 0$, it means that $u_x(t_0) = 0$ as a transition from 0 to 1 is required in phase x within T_s. If, on the other hand, $\Delta u_x < 0$, then it holds that $u_x(t_0) = 1$ as phase x needs to switch from 1 to 0. Following the same principle, the feasible switch positions—and eventually $u_x(t_0)$—for the case of $v_{\mathrm{db},x} < 0$ are defined. The switching transitions and initial single-phase switch position are summarized in Table II. Moreover, Fig. 2 provides an illustrative example of the discussed concept. Therein, it is assumed that $v_{\mathrm{db},a}, v_{\mathrm{db},c} \geq 0$, whereas $v_{\mathrm{db},b} < 0$. Furthermore, the sign of $\Delta\boldsymbol{u}_{abc}(k)$ for the first sampling interval is assumed to be positive, implying a negative sign for the second T_s.

Finally, with the information of the initial switch position $\boldsymbol{u}_{abc}(t_0)$ and possible switching transitions, the feasible set of switching sequences is constructed by enumerating the six possible sequences shown in Table I. Let $z \in \{1, 2, \ldots, 6\}$ denote the number of sequence, the feasible set consists of only six candidate switching sequences $\boldsymbol{U}_z = [\boldsymbol{u}_{abc}^T(t_0)\ \boldsymbol{u}_{abc,z}^T(t_1)\ \boldsymbol{u}_{abc,z}^T(t_2)\ \boldsymbol{u}_{abc}^T(t_3)]^T$.

C. Optimization Problem

In order to have a convex optimization problem, the objective function is simplified by capturing only the output error at the switching instants and at the end of the sampling interval, see [22]. This leads to

$$J = \sum_{i=1}^{3} \left\| \boldsymbol{y}_{\mathrm{ref}}(t_i(k)) - \boldsymbol{y}(t_i(k)) \right\|_{\boldsymbol{Q}}^2 \\ + \left\| \boldsymbol{\Lambda}(\boldsymbol{y}_{\mathrm{ref}}(T_s(k)) - \boldsymbol{y}(T_s(k))) \right\|_{\boldsymbol{Q}}^2, \tag{13}$$

where the diagonal positive definite matrix $\boldsymbol{\Lambda} \succ 0$ is introduced to more heavily penalize the output error at the end of the sampling interval. Note that $\boldsymbol{y}_{\mathrm{ref}}(T_s(k)) \equiv \boldsymbol{y}_{\mathrm{ref}}(k+1)$ and $\boldsymbol{y}(T_s(k)) \equiv \boldsymbol{y}(k+1)$. By doing so, the output error at the sampling instants is always kept close to zero, which effectively eliminates the undesired low-frequency harmonics [22].

---

[7] Note that the discrete state-space model of the IM can be obtained with forward Euler discretization, i.e., $\boldsymbol{A}_m = \boldsymbol{I} + \boldsymbol{F}_m T_s$ and $\boldsymbol{B}_m = \boldsymbol{G}_m T_s$.
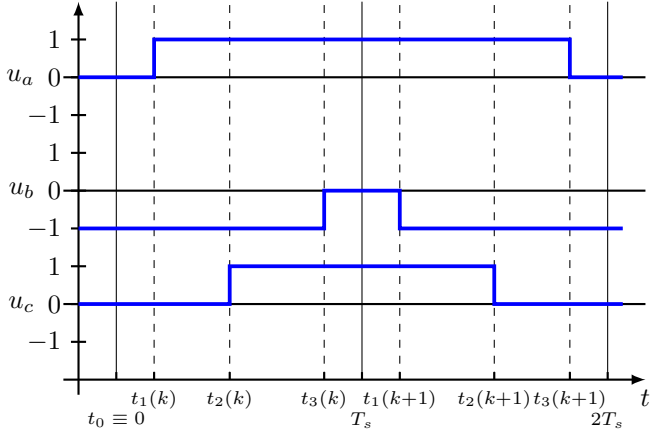
(a) Three-phase switching sequence.
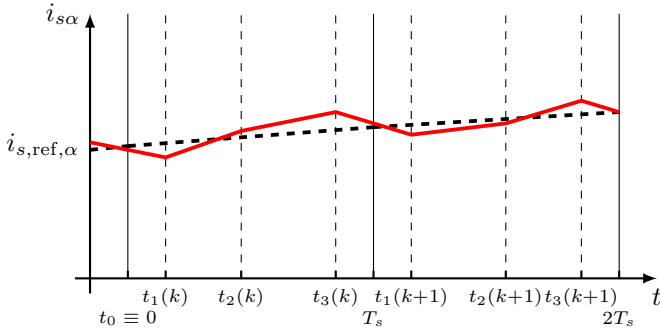
(b) Stator current (α-component).

Fig. 2: Example of one switching sequence and the corresponding stator current.

To find the optimal switching instants $\boldsymbol{t}^*$ and switching sequence $\boldsymbol{U}^*$, the evolution of the output $\boldsymbol{y}$ for each possible switching sequence $\boldsymbol{U}_z$ needs to be computed. Given that the sampling interval T_s is much smaller than the fundamental period T_1, i.e., $T_s \ll T_1$, the corresponding output gradients, given by

$$
\begin{aligned}
\boldsymbol{m}(t_i(k)) &= \frac{\boldsymbol{y}(k+1) - \boldsymbol{y}(k)}{T_s} \\
&= \frac{\boldsymbol{C}((\boldsymbol{A} - \boldsymbol{I})\boldsymbol{x}(k) + \boldsymbol{B}\boldsymbol{u}_{abc}(t_i(k)))}{T_s} .
\end{aligned}
\tag{14}
$$

can be utilized to predict the evolution of the system output. This yields

$$
\boldsymbol{y}(t_{i+1}(k)) = \boldsymbol{y}(t_i(k)) + \boldsymbol{m}(t_i(k))(t_{i+1}(k) - t_i(k)), \tag{15}
$$

with $i \in \{0, 1, 2, 3\}$ and $t_4 = T_s$.

In the same manner, the output reference is assumed to evolve linearly within one sampling interval, i.e., it evolves with the gradient

$$
\boldsymbol{m}_{\mathrm{ref}}(k) = \frac{\boldsymbol{y}_{\mathrm{ref}}(k+1) - \boldsymbol{y}_{\mathrm{ref}}(k)}{T_s} , \tag{16}
$$

Hence, the output reference over this sampling interval is

$$
\boldsymbol{y}_{\mathrm{ref}}(t) = \boldsymbol{y}_{\mathrm{ref}}(k) + \boldsymbol{m}_{\mathrm{ref}}(k)\, t . \tag{17}
$$

An example of the evolution of the stator current for a given switching sequence (the depicted sequence is $a \to c \to b$)

Algorithm 1 QP Algorithm for Direct MPC

```
 1: function  t_z = GRADPROJ (H, f, t_0, L, μ, tol)
 2:     q = μ/L
 3:     y_0 = t_0
 4:     α_0 = (√((L − μ)² + 4L) − (L − μ))/2
 5:     for κ = 0, 1, …  do
 6:         t_{κ+1} = P_Ω(y_κ − (H y_κ − f)/L)
 7:         if ‖t_{κ+1} − t_κ‖ ≤ tol then
 8:             t_z = t_{κ+1}
 9:             break
10:         end if
11:         α_{κ+1} = (√((α_κ² − q)² + 4α_κ²) − (α_κ² − q))/2
12:         β_κ = (α_κ(1 − α_κ))/(α_κ² + α_{κ+1})
13:         y_{κ+1} = t_{κ+1} + β_κ(t_{κ+1} − t_κ)
14:     end for
15:     return t_z
16: end function
```

and its reference are shown in Fig. 2. Note that the current reference is generated by an outer loop, and the reference of the NP potential $v_{n,\mathrm{ref}}$ is zero.

Based on the above, the objective function can be written in the following vector form

$$
J = \left\| \boldsymbol{r} - \boldsymbol{M}\boldsymbol{t} \right\|_{\tilde{\boldsymbol{Q}}}^2 , \tag{18}
$$

where $\tilde{\boldsymbol{Q}} = \mathrm{diag}(\boldsymbol{Q}, \ldots, \boldsymbol{Q})$, while the vector $\boldsymbol{r} \in \mathbb{R}^{12}$ and the matrix $\boldsymbol{M} \in \mathbb{R}^{12 \times 3}$ are given in the appendix. Therefore, for each switching sequence $\boldsymbol{U}_z$, with $z \in \{1, 2, \ldots, 6\}$, the optimization problem that is solved in real time is

$$
\begin{aligned}
&\underset{\boldsymbol{t} \in \mathbb{R}^3}{\mathrm{minimize}} \quad \|\boldsymbol{r} - \boldsymbol{M}\boldsymbol{t}\|_{\tilde{\boldsymbol{Q}}}^2 \\
&\text{subject to} \quad 0 \le t_1(k) \le t_2(k) \le t_3(k) \le T_s .
\end{aligned}
\tag{19}
$$

This problem is a convex constrained QP because the Hessian matrix $\boldsymbol{H} = \boldsymbol{M}^T \boldsymbol{M}$ is always positive definite. Therefore, it can be efficiently solved with the in-house QP algorithm developed in [25]. This gradient-based algorithm, developed to exploit the structure of (19), has the advantageous feature that it can detect unsuited $\boldsymbol{U}_z$ with a simple one-step gradient projection method. As a result, at most two QPs (19) need to be solved in real time, thus greatly reducing the computational burden of the proposed direct MPC scheme. Note that in [25] the step size of the gradient method is chosen according to the Barzilai and Borwein (BB) method [28], due to its robustness to ill-posed QPs. However, the Hessian matrix $\boldsymbol{H}$ in this work is always well conditioned, i.e., its condition number—which is defined as the largest eigenvalue of the Hessian matrix divided by its smallest eigenvalue—is relatively small. Therefore, the Nesterov fast gradient method [29], [30] is adopted in this work to calculate the step size, resulting in a more efficient convergence. Algorithm 1 shows the pseudocode of the modified QP algorithm, where the so-called Lipschitz constant L and convexity parameter μ are the maximum and minimum eigenvalues of the Hessian matrix $\boldsymbol{H}$, respectively. Moreover, the vector $\boldsymbol{f}$ is defined as $\boldsymbol{f} = 2\boldsymbol{M}^T \boldsymbol{r}$. Besides, P_Ω denotes the operation that projects any variable onto the

Algorithm 2 Fixed Switching Frequency Direct MPC

    Given $\boldsymbol{y}_{\mathrm{ref}}(k)$, $\boldsymbol{y}_{\mathrm{ref}}(k+1)$ and $\boldsymbol{x}(k)$
1: Compute the deadbeat solution $\boldsymbol{v}_{\mathrm{db},abc}$ according to (12)
2: Enumerate the possible switching sequences $\boldsymbol{U}_z$, $z \in \{1, 2, \ldots, 6\}$, based on $\boldsymbol{v}_{\mathrm{db},abc}$ and the sign of the switching transitions $\Delta\boldsymbol{u}_{abc}$
3: For each $\boldsymbol{U}_z$:
    Detect if $\boldsymbol{U}_z$ is unsuited;
    If not, solve the QP (19). This yields $\boldsymbol{t}_z$ and J_z.
4: Solve optimization problem (20). This yields $\boldsymbol{t}^*$ and $\boldsymbol{U}^*$.
    Return $\boldsymbol{t}^*(k)$ and $\boldsymbol{U}^*(k)$.
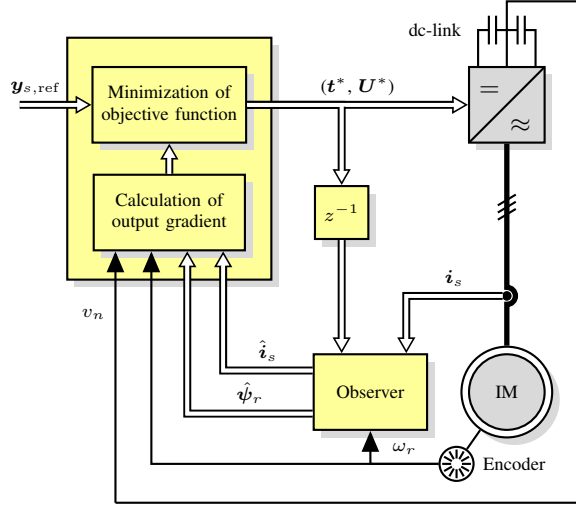
Fig. 3: Fixed switching frequency direct MPC for a three-phase NPC inverter driving an IM.

feasible region Ω, $\boldsymbol{t}_0 \in \Omega$ is the initial point, and $tol \in \mathbb{R}^+$ is the tolerance. For the details on the projection algorithm P_Ω and the definition of other variables in Algorithm 1, please refer to [25, Section IV].

In a last step the (globally) optimal switching instants $\boldsymbol{t}^*$ and sequence $\boldsymbol{U}^*$ is found by comparing the cost J_z of each switching sequence, i.e., the following problem is solved

$$\underset{z \in \{1,2,\ldots,6\}}{\text{minimize}} \quad J_z . \tag{20}$$

Finally, the optimal switching sequence $\boldsymbol{U}^*$ is applied to the inverter at the corresponding optimal switching instants $\boldsymbol{t}^*$.

The proposed direct MPC scheme is summarized in the pseudocode provided in Algorithm 2, while the block diagram is shown in Fig. 3. Finally it should be mentioned that a Kalman filter (KF) is implemented to deal with model uncertainties, parameter variations, measurement noise, etc., see [25, Section III-D] and references therein for more details on the design of the KF.

IV. PERFORMANCE EVALUATION

The performance of the proposed direct MPC scheme is examined in the laboratory with a three-phase 3L-NPC inverter driving an IM, as shown in Fig. 1. The inverter is supplied by a stiff dc source and the NP is floating. The real-time control platform is a dSPACE SCALEXIO system, consisting
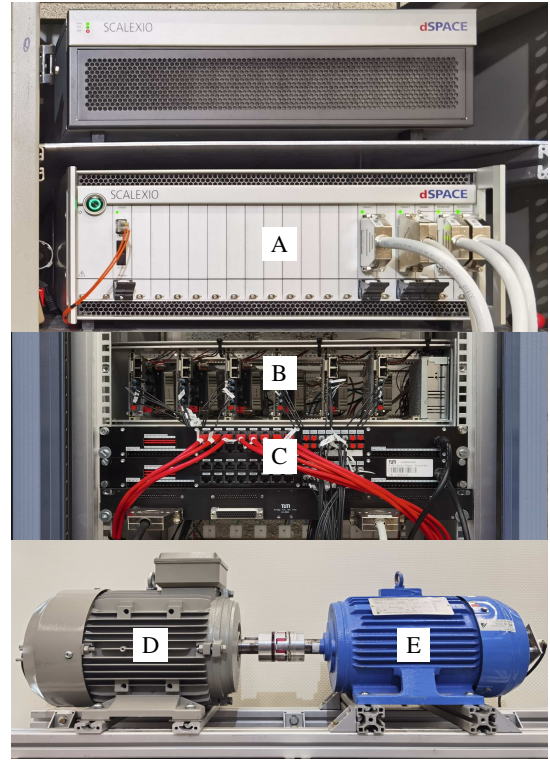
Fig. 4: Setup of the electrical drives test bench. A: dSPACE SCALEXIO real-time control system, B: Back-to-back 3L-NPC converters, C: Interface, D: IM, E: PMSM

TABLE III: Rated values of the induction machine.

Parameter	Symbol	SI Value
Rated voltage	V_R	400 V
Rated current	I_R	8.73 A
Rated stator frequency	f_{sR}	50 Hz
Rated rotor speed	ω_{mR}	1430 rpm
Rated power	P_R	4 kW

TABLE IV: System parameters in the SI and the p.u. system.

Parameter	SI (p.u.) symbol	SI (p.u.) value
Stator resistance	R_s (R_s)	2.94 Ω (0.11)
Rotor resistance	R_r (R_r)	0.67 Ω (0.024)
Stator leakage inductance	L_{ls} (X_{ls})	8.45 mH (0.096)
Rotor leakage inductance	L_{lr} (X_{lr})	8.45 mH (0.096)
Mutual inductance	L_m (X_m)	195.25 mH (2.26)
Number of pole pairs	p	2
Dc-link voltage	V_{dc} (V_{dc})	650 V (1.99)
Dc-link capacitance	C_{dc} (X_{dc})	1.6 mF (13.43)

of a $4\,\mathrm{GHz}$ Intel XEON processor and a Xilinx Kintex-7 field-programmable gate array (FPGA). The controller is implemented on the processor, and the data acquisition and generation of the switching signals are done on the FPGA. The experimental setup is shown in Fig. 4. The rated values of the IM and the parameters of the system are given in Tables III and IV, respectively. For the examined scenarios, the weighting matrices are chosen as $\boldsymbol{Q} = \mathrm{diag}(1, 1, 5)$ and $\boldsymbol{\Lambda} = \mathrm{diag}(10, 10, 10)$. Finally, all results are shown in the p.u. system.
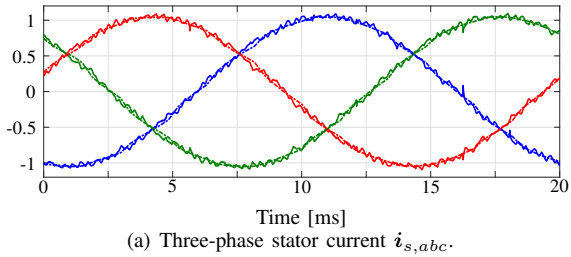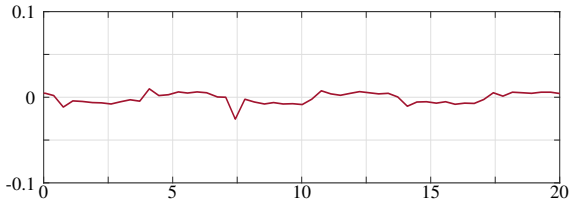
(a) Three-phase stator current $\boldsymbol{i}_{s,abc}$.
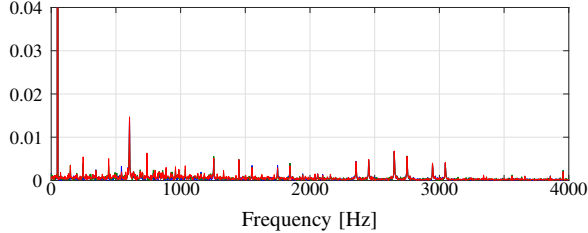
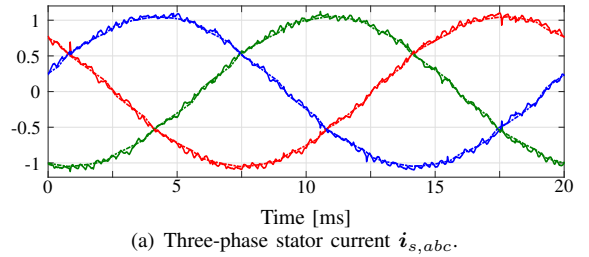(b) Stator current harmonic spectrum. The THD is 3.60%.
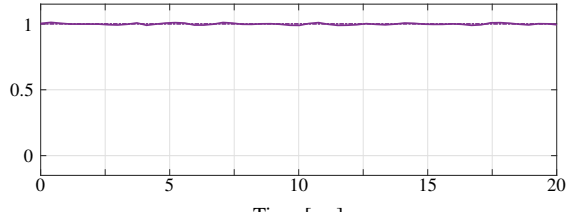
(c) Electromagnetic torque.

(d) The neutral point potential v_n.

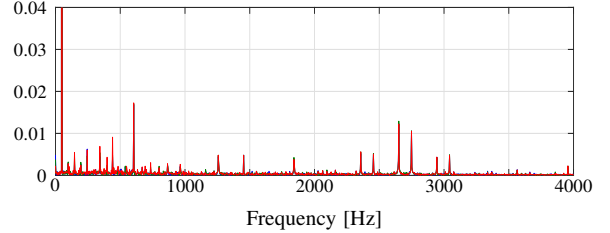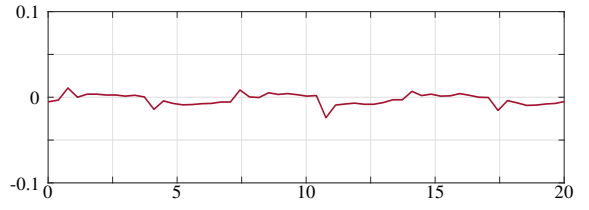Fig. 5: Experimental results of direct MPC at steady-state operation, $f_{\mathrm{sw}} = 700\,\mathrm{Hz}$.

(a) Three-phase stator current $\boldsymbol{i}_{s,abc}$.

(b) Stator current harmonic spectrum. The THD is 3.81%.

(c) Electromagnetic torque.

(d) The neutral point potential v_n.

Fig. 6: Experimental results of FOC at steady-state operation, $f_{\mathrm{sw}} = 700\,\mathrm{Hz}$.

A. Steady-State Operation

The steady-state performance throughout this section is examined while the IM is operating at nominal speed and rated torque, implying a fundamental frequency of $f_1 = 50\,\mathrm{Hz}$ and electromagnetic torque $T_e = 1\,\mathrm{p.u.}$ Moreover, the sampling frequency is chosen as $f_s = 2700\,\mathrm{Hz}$ such that a device switching frequency of $f_{\mathrm{sw}} = 700\,\mathrm{Hz}$ results.[8] Fig. 5 shows the performance of the drive system controlled by the proposed direct MPC. As shown in 5(a), the three-phase stator current $\boldsymbol{i}_{s,abc}$, measured by an oscilloscope with a sampling frequency of $50\,\mathrm{kHz}$, tracks its reference with no steady-state error and low harmonic distortions. The stator current harmonic spectrum is shown in 5(b), while the total harmonic distortion

---

[8]The proposed direct MPC method ensures that there is one switching transition in each phase leg per T_s. This means that T_s is akin to the modulation half-cycle of CB-PWM/SVM. Considering a three-level NPC converter, this implies that there are $T_1/(2T_s) + 1$ switching transitions in one fundamental period T_1. As two consecutive switching transitions give rise to one pulse, the switching frequency relates to T_s (f_s) according to $f_{\mathrm{sw}} = 1/(4T_s) + 1/(2T_1) = f_s/4 + f_1/2$.

(THD) is 3.60%, which is relatively low for a low-voltage machine at the examined switching frequency. In addition, the harmonic power is mainly concentrated at the odd non-triplen multiples of the fundamental frequency, which are caused by the switching nature of the inverter. Besides, some low-frequency harmonics can also be observed—with the 12th harmonic being the prominent—which are caused by the slotting and saturation effects in the IM [31]. Moreover, the NP potential of the inverter is well balanced, with the deviation being kept always within 3%, as shown in Fig. 5(d).

For comparison purposes, FOC with PI controllers and CB-PWM is also implemented. The CB-PWM is with asymmetric sampling and a suitable common-mode signal is injected to achieve equivalence with SVM [32]. As for the parameters of the PIs, they are tuned according to the modulus optimum method [33]. Furthermore, the NP potential is balanced by manipulating the CMV in the three-phase modulation signal. The CMV reference is generated by a simple PI-based closed-loop controller presented in [6]. The operating conditions, sampling frequency, and thus switching frequency, are the
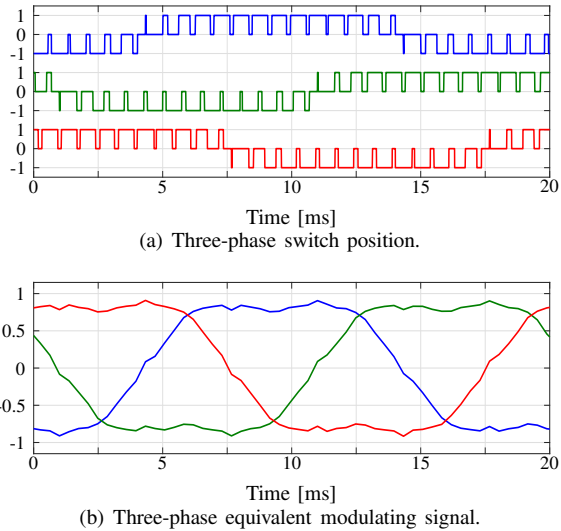
(a) Three-phase switch position.

(b) Three-phase equivalent modulating signal.

Fig. 7: Three-phase switch position and equivalent modulating signal of direct MPC at steady state, $f_{\mathrm{sw}} = 700\,\mathrm{Hz}$.

(a) Three-phase switch position.

(b) Three-phase modulating signal.

Fig. 8: Three-phase switch position and modulating signal of FOC at steady state, $f_{\mathrm{sw}} = 700\,\mathrm{Hz}$.

Fig. 9: Trade-off between current THD and switching frequency for the proposed direct MPC (blue, solid line), FOC (black, dashed line), FCS-MPC1 (green, dotted line), and FCS-MPC2 (red, dash-dotted line).

same as those of direct MPC. As shown in Fig. 6, FOC achieves very similar steady-state performance, i.e., the three-phase stator current tracks its reference accurately and the NP potential is well balanced. However, the stator current has a slightly higher ripple especially of low frequency, as shown in Fig. 6(b), resulting in a slightly increased THD, i.e., 3.81% compared to 3.60% of the direct MPC scheme. This can be explained by the fact that the linear PI controllers of FOC cannot quickly compensate for the disturbance caused by the NP potential ripple and the nonlinear effects in the IM, e.g., slotting and saturation effects. As a result, low-frequency harmonics (e.g., from 5th and up to 13th, with the 12th again being the dominant) are pronounced in the harmonic spectrum of FOC. In contrast, the direct MPC strategy, thanks to its high control bandwidth, can effectively suppress these harmonics caused by the floating NP and the nonlinear effects of the IM.

Furthermore, the three-phase switch position $\boldsymbol{u}_{abc}$ generated by direct MPC and FOC is shown in Figs. 7(a) and 8(a), respectively. As shown, direct MPC yields a very similar switching pattern as that of FOC with SVM in steady-state operation, i.e., each phase switches one level up or down within one T_s, although there is no explicit modulation stage. The latter implies that there is no modulating signal in direct MPC. However, to provide more insight into the workings of the proposed algorithm, we introduce the variable $\bar{\boldsymbol{u}}_{abc} = (\sum_{i=0}^{3} \boldsymbol{u}_{abc}(t_i)\tilde{t}_i)/T_s$, where $\tilde{t}_i = t_{i+1} - t_i$, with $i \in \{0,1,2,3\}$ and $t_4 = T_s$, which can be interpreted as an equivalent modulating signal. As can be seen in Figs. 7(b) and 8(b), the equivalent modulating signal of the direct MPC scheme is similar to the modulating signal of FOC with SVM. It is worth noting that $\bar{\boldsymbol{u}}_{abc}$ has the shape of a modulating signal injected with a CMV signal. This is an inherent feature of the proposed method as no external signals are injected to the output of the MPC algorithm.

Finally, the tradeoff curves between the current THD and the switching frequency for direct MPC and FOC are shown in Fig. 9. Moreover, two conventional FCS-MPC methods are
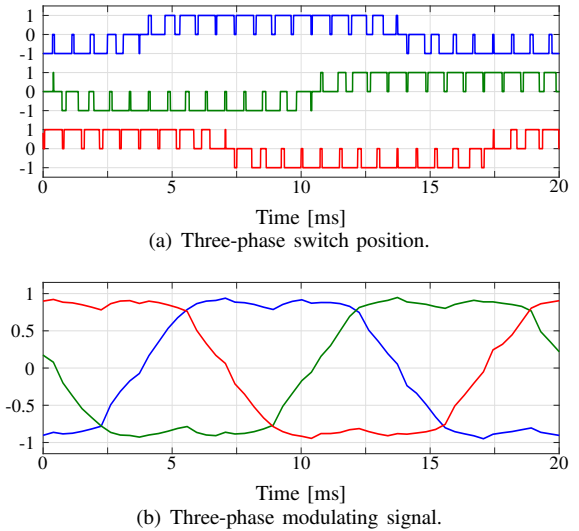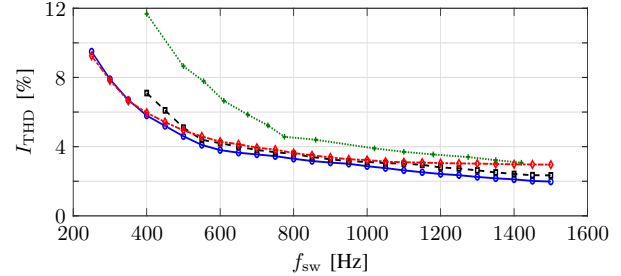
also implemented for comparison purposes. Specifically, the first FCS-MPC method (referred to as FCS-MPC1) has the objective function

$$J = \|\boldsymbol{i}_{s,\mathrm{ref}}(k+1) - \boldsymbol{i}_s(k+1)\|_1 + \lambda_{v_n}|v_{n,\mathrm{ref}}(k+1) - v_n(k+1)|\,,$$

i.e., it does not penalize the switching effort and uses the ℓ_1-norm, while the switching frequency is adjusted by modifying the sampling interval T_s. The objective function of the second FCS-MPC method (FCS-MPC2) is based on the ℓ_2-norm, and penalizes the control effort, i.e.,[9]

$$\begin{aligned} J =& \|\boldsymbol{y}_{s,\mathrm{ref}}(k+1) - \boldsymbol{y}_s(k+1)\|_2^2 + \\ & \lambda_{v_n}(v_{n,\mathrm{ref}}(k+1) - v_n(k+1))^2 + \lambda_u\|\Delta\boldsymbol{u}_{abc}(k)\|_2^2\,. \end{aligned}$$

For this method the sampling frequency is set equal to $f_s = 16\,\mathrm{kHz}$, while the switching frequency is adjusted by tuning the weighting factor λ_u in the objective function.

As can be seen from Fig. 9, FCS-MPC1 yields the worst steady-state performance over the whole range of the examined switching frequencies. Moreover, both the proposed direct MPC and FOC achieve lower current THD than FCS-MPC2 for $f_{\mathrm{sw}} \in [550, 1550]\,\mathrm{Hz}$. For FCS-MPC2 to achieve lower values of THD much higher sampling frequencies would be
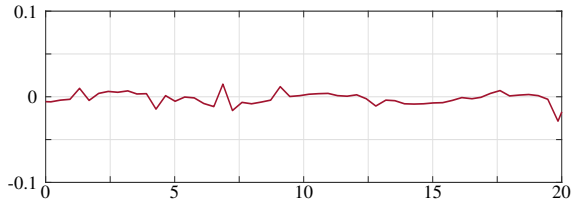

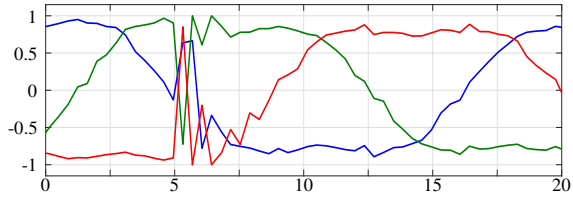[9]The reader is referred to [11] for insights into the discussed designs of FCS-MPC.
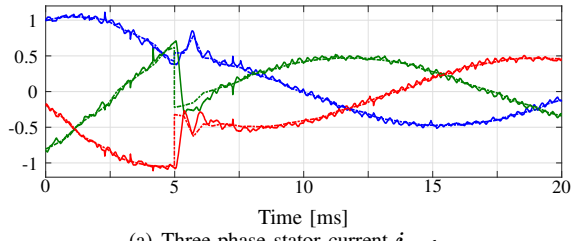
(a) Three-phase stator current $\boldsymbol{i}_{s,abc}$.
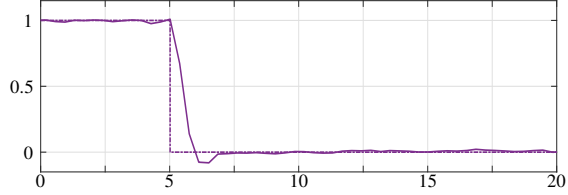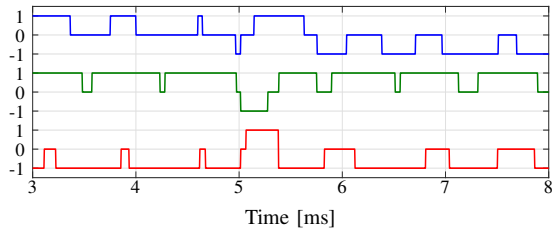

(b) Electromagnetic torque.

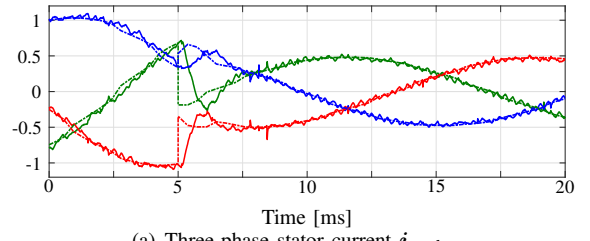(c) The neutral point potential v_n.

(d) Three-phase equivalent modulating signal.
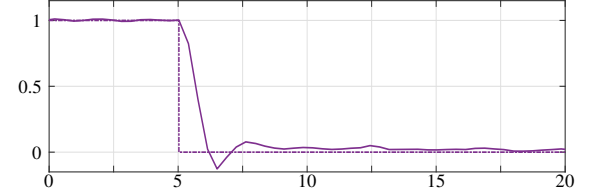

(e) Three-phase switch position (zoomed in at transient).

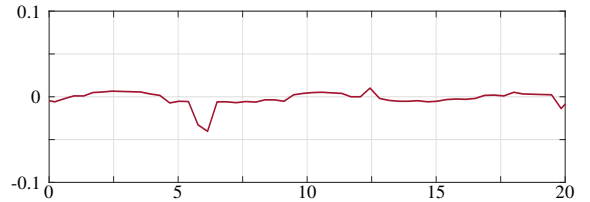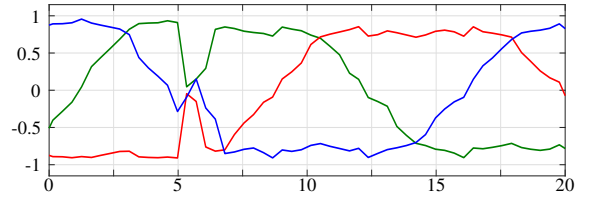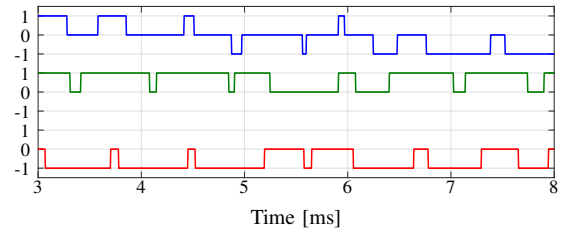Fig. 10: Experimental results of direct MPC at a torque reference step-down transient.

(a) Three-phase stator current $\boldsymbol{i}_{s,abc}$.

(b) Electromagnetic torque.

(c) The neutral point potential v_n.
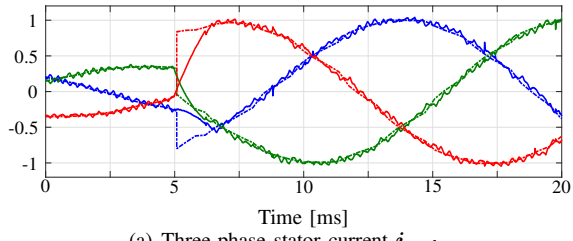

(d) Three-phase equivalent modulating signal.

(e) Three-phase switch position (zoomed in at transient).

Fig. 11: Experimental results of FOC at a torque reference step-down transient.

required which would render its real-time implementation challenging [11]. Hence, these results demonstrate the advantages of the proposed control method as it is suitable for a wider range of switching frequencies. This observation is also supported by the fact that the presented algorithm outperforms FOC over the whole range of switching frequencies. Moreover, as can be seen, at the low switching frequency range ($f_{sw} < 550\,\text{Hz}$), the current THD of FOC increases significantly as f_{sw} decreases, while FOC becomes unstable at $f_{sw} < 400\,\text{Hz}$. This is in stark contrast with the performance of the proposed direct MPC scheme and FCS-MPC2, which

still produce relatively low current THD at such low switching frequencies.

B. Performance During Transients

The transient behavior of the proposed direct MPC is tested by commanding the torque reference to step from $T_{e,\text{ref}} = 1$ to 0 p.u., and from $T_{e,\text{ref}} = 0$ to 1 p.u., while operating at the same switching frequency as before, i.e., $f_{sw} = 700\,\text{Hz}$. As shown in Fig. 10, where the torque reference step-down scenario is depicted, the direct MPC scheme quickly regulates the current—and thus the torque—to their new references,
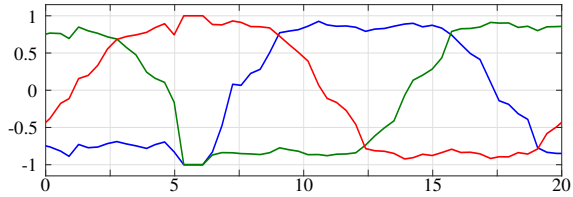
(a) Three-phase stator current $\boldsymbol{i}_{s,abc}$.
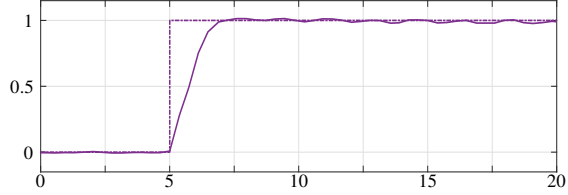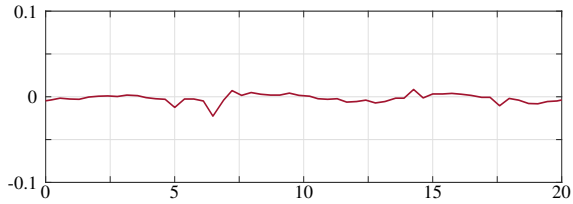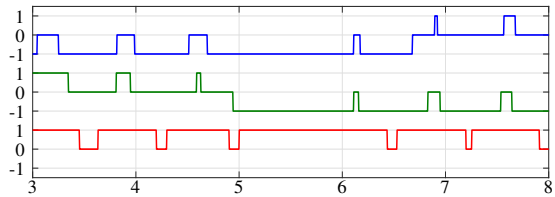

(b) Electromagnetic torque.
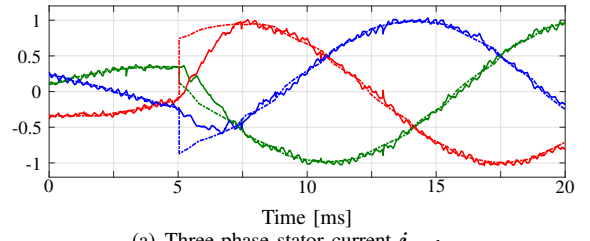

(c) The neutral point potential v_n.

(d) Three-phase equivalent modulating signal.

(e) Three-phase switch position (zoomed in at transient).

Fig. 12: Experimental results of direct MPC at a torque reference step-up transient.

(a) Three-phase stator current $\boldsymbol{i}_{s,abc}$.

(b) Electromagnetic torque.

(c) The neutral point potential v_n.
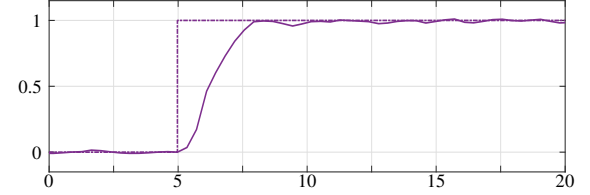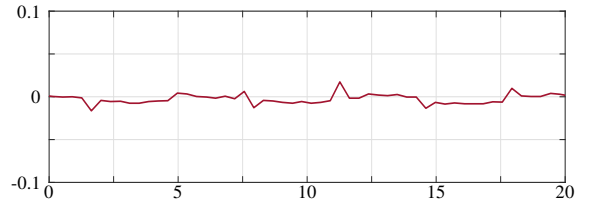

(d) Three-phase equivalent modulating signal.

(e) Three-phase switch position (zoomed in at transient).

Fig. 13: Experimental results of FOC at a torque reference step-up transient.

within around $2\,\mathrm{ms}$, while keeping the NP potential well balanced. Such a favorable behavior can be achieved due to the polarity reversal of the deadbeat solution $\boldsymbol{v}_{\mathrm{db},abc}^{*}$ at the beginning of the transient. As a result, the switch position $\boldsymbol{u}_{abc}(t_0)$ at the beginning of the transient is adjusted to reflect this change. In doing so, such switch positions and corresponding switching times are computed that result in the shortest settling time possible. This point is clearly shown in Fig. 10(e), where the three-phase switch position is depicted during the transient. Moreover, the equivalent modulating signal illustrated in Fig. 10(d) further highlights this behavior.
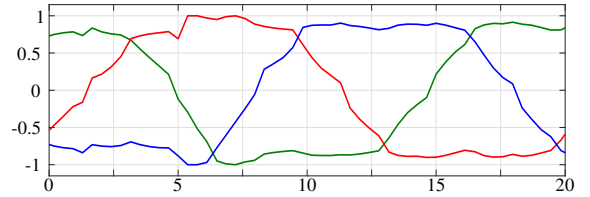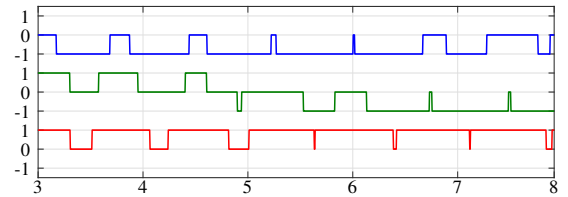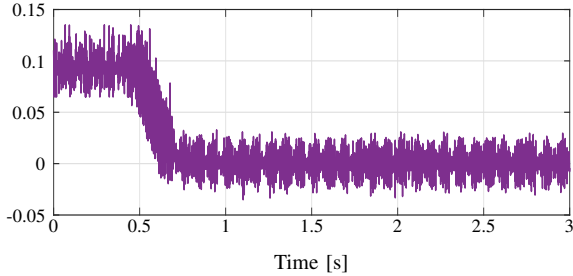
In comparison, the performance of FOC under the same scenario is not as good, see Fig. 11. As can be seen, FOC takes a significantly longer time (around $4\,\mathrm{ms}$) to settle to the new operating point, due to the fact that the available dc-link voltage is underutilized, as a polarity reversal is not achieved. Besides, a spike on the NP potential can be observed during the transient, see Fig. 11(c).

As for the torque reference step-up change, direct MPC pushes the switching instants to the limits, i.e., at the beginning or end of each T_s, such that only the switch position (i.e., $\boldsymbol{u}_{abc}(t_0)$ or $\boldsymbol{u}_{abc}(t_3)$) that regulates the current and torque

(a) Proposed direct MPC.
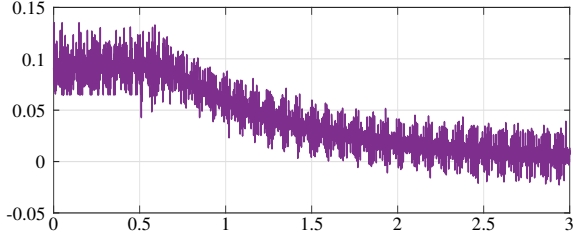
(b) Natural balancing.

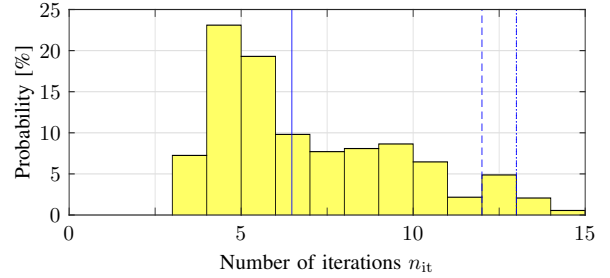Fig. 14: NP potential balancing.

Fig. 15: Probability distribution of the number of iteration steps required by the QP algorithm. The average number of iterations is indicated by the solid vertical line. The 95, 98, and 99 percentiles are shown as dashed, dashed-dotted, and dotted vertical lines, respectively.

Fig. 16: Probability distribution of the turnaround time $t_{\mathrm{ta,tot}}$. The average turnaround time is indicated by the solid vertical line. The 95, 98, and 99 percentiles are shown as dashed, dashed-dotted, and dotted vertical lines, respectively.
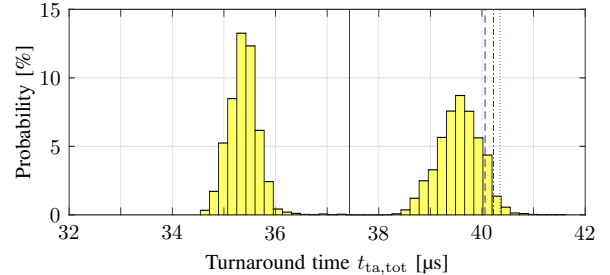
to their new references as fast as possible is applied for the whole sampling interval, see Fig. 12. By doing so, the available dc-link voltage is fully utilized, and the settling time is only limited by the physical limits of the system. In contrast, FOC cannot push the modulating signal immediately to the maximum limit due to its relatively low bandwidth limited by the integrating element in the controller. As a result, the direct MPC scheme achieves a significantly faster settling time of about 2 ms, which is almost half of that required by FOC, see Fig. 13.

C. Neutral Point Potential Balancing

To further verify the active NP balancing capability of the proposed direct MPC strategy, the drive system is tested at nominal speed but with no mechanical load, i.e., there is only magnetizing current. This working condition is recognized as a critical one for 3L-NPC inverters [6], [8]. For this test a 0.1 p.u. offset is initially introduced to the NP potential. As can be seen, direct MPC regulates the NP potential quickly to zero within around 0.2 s, see Fig. 14(a). On the other hand, FOC cannot exhibit such a favorable balancing property. This is due to the fact that the PI-based NP controller in FOC tends to become unstable under no-load conditions [6]. For this reason, it is typical to disable the NP controller at zero PF such that natural balancing mechanism of the NP potential is enabled [34]. As shown in Fig. 14(b), the NP potential balancing is achieved in about 2 s under such conditions. This time is one order of magnitude longer than that required by the presented direct MPC scheme. These results clearly demonstrate the advantages of the inherent active NP potential balancing capability of the proposed control method.

D. Computational Burden

The main challenge of the real-time implementation of the direct MPC scheme is the relatively high computational burden caused by solving the QP problems. Thanks to the efficient projection algorithm developed in [25], and its refinement based on the fast Nesterov gradient method [29], the computational burden is kept modest. To quantify this, Fig. 15 shows the probability distribution of the number of iteration steps n_{it} required by the developed QP solver to find the solution. As can be seen, at most 15 iterations are required. To further elucidate this point, Fig. 16 depicts the turnaround time $t_{\mathrm{ta,tot}}$ of the whole direct MPC scheme in the dSPACE. As can be seen, the probability distribution of the turnaround time $t_{\mathrm{ta,tot}}$ is concentrated mainly around two locations, depending on whether one or two QPs are solved in real time. The number of QPs solved depends on the geometry of the underlying optimization problem and the ability of the solver to exclude suboptimal solutions at a very early stage. Nevertheless, in the worst-case scenario, only two QPs need to be solved, thus greatly alleviating the computational complexity of the proposed optimal control method. As a result, the maximum turnaround time of the developed direct MPC algorithm is only $41.6\,\mu s$, see Table V where the average and maximum turnaround times of the four discussed control algorithms are summarized. This time is much smaller than the sampling interval T_s, which in the case of $f_{\mathrm{sw}} = 700\,\mathrm{Hz}$ is about $370\,\mu s$, meaning that only about 10% of the available time is used to execute the controller. In contrast to that, e.g., FCS-MPC2, whose sampling time is $62.5\,\mu s$, requires about $20/62.5 = 32\%$ of the available time for the controller.

V. CONCLUSIONS

This article proposed a direct MPC strategy for a three-phase 3L-NPC inverter driving an IM. In contrast to conventional FOC with SVM, the direct MPC scheme directly

TABLE V: The average/maximum turnaround time $t_{\text{ta,ave}}/t_{\text{ta,max}}$ of the four discussed control algorithms running on dSPACE.

Turnaround time	FOC	FCS-MPC1	FCS-MPC2	Direct MPC
average $t_{\text{ta,ave}}$ (µs)	15.2	16.4	16.5	37.4
max $t_{\text{ta,max}}$ (µs)	18.2	19.6	19.8	41.6

manipulates the inverter switch positions to fully exploit the discrete nature of the inverter such that superior performance is achieved both at steady-state and transient operating conditions. To this aim, the direct MPC scheme implicitly introduces a fixed modulation cycle and symmetric switching patterns, i.e., akin to SVM, so that a constant switching frequency and a discrete output harmonic spectrum with low THD are achieved at steady state. Moreover, the direct MPC scheme exploits the characteristic of direct control schemes during transients, i.e., it directly manipulates the inverter switch positions such that the available dc-link voltage is fully utilized, leading to very short settling times.

Moreover, thanks to the versatility and conceptual simplicity of the gradient-based model, the direct MPC scheme can easily formulate the IM current control and inverter NP balancing problems into one constrained optimization problem. Conventionally, the NP balancing is achieved by an additional control loop due to its nonlinear dynamics. However, these cascaded/parallel structures reduce the bandwidth of the controller, or they can even cause closed-loop stability issues, especially at challenging operating conditions, e.g., a zero PF. On the other hand, the proposed direct MPC scheme addresses all the control objectives in one computational stage while operating the drive system at its physical operation limits. Thus, the most favorable performance is ensured over the whole operating regime, while the structure of the controller remains simple.

Finally, a mechanism is proposed to keep the computational complexity of the developed optimal control method modest. Specifically, the feasible set of candidate solutions is limited depending on the polarity of the deadbeat solution, and the candidate switching patterns are determined by considering the allowable switching transitions. As shown, this technique, combined with the efficient in-house solver tailored to the needs of the formulated QP underlying direct MPC, enable the real-time implementation of the proposed algorithm as at most two QPs need to be solved at each sampling interval. As a result, the aforementioned benefits of the discussed control method were verified in a real-world setting.

APPENDIX

The matrices in (7) are

$$
F(u_{abc}(t)) = \begin{bmatrix} F_m & \begin{bmatrix} -\frac{X_r}{D} K|u_{abc}| \\ \mathbf{0}_{2\times 1} \end{bmatrix} \\ \begin{bmatrix} \frac{1}{2X_{\text{dc}}} |u_{abc}|^T K^{-1} & \mathbf{0}_{1\times 2} \end{bmatrix} & 0 \end{bmatrix},
$$

$$
G = \frac{v_{\text{dc}}}{2} G_m K, \ C = \begin{bmatrix} C_m & \mathbf{0}_{2\times 1} \\ \mathbf{0}_{1\times 4} & 1 \end{bmatrix}.
$$

where

$$
F_m = \begin{bmatrix} -\frac{1}{\tau_s} & 0 & \frac{X_m}{\tau_r D} & \omega_r \frac{X_m}{D} \\ 0 & -\frac{1}{\tau_s} & -\omega_r \frac{X_m}{D} & \frac{X_m}{\tau_r D} \\ \frac{X_m}{\tau_r} & 0 & -\frac{1}{\tau_r} & -\omega_r \\ 0 & \frac{X_m}{\tau_r} & \omega_r & -\frac{1}{\tau_r} \end{bmatrix},
$$

$$
G_m = \frac{X_r}{D} \begin{bmatrix} 1 & 0 \\ 0 & 1 \\ 0 & 0 \\ 0 & 0 \end{bmatrix}, \ C_m = \begin{bmatrix} 1 & 0 & 0 & 0 \\ 0 & 1 & 0 & 0 \end{bmatrix}.
$$

The matrices in (18) are

$$
r = \begin{bmatrix} y_{\text{ref}}(t_0) - y(t_0) \\ y_{\text{ref}}(t_0) - y(t_0) \\ y_{\text{ref}}(t_0) - y(t_0) \\ \Lambda(y_{\text{ref}}(T_s) - y(t_0) - m(t_3)T_s) \end{bmatrix}
$$

and

$$
M = \begin{bmatrix} m_{t_0} & \mathbf{0}_3 & \mathbf{0}_3 \\ m_0 & m_{t_1} & \mathbf{0}_3 \\ m_0 & m_1 & m_{t_2} \\ \Lambda m_0 & \Lambda m_1 & \Lambda m_2 \end{bmatrix}
$$

with

$$
m_{t_i} = m(t_i) - m_{\text{ref}}
$$
$$
m_i = m(t_i) - m(t_{i+1})
$$

where $i \in \{0, \ 1, \ 2\}$.

REFERENCES

[1] A. Nabae, I. Takahashi, and H. Akagi, "A new neutral-point-clamped PWM inverter," *IEEE Trans. Ind. Appl.*, vol. IA-17, no. 5, pp. 518–523, Sep./Oct. 1981.

[2] H. Abu-Rub, J. Holtz, J. Rodriguez, and G. Baoming, "Medium-voltage multilevel converters—State of the art, challenges, and requirements in industrial applications," *IEEE Trans. Ind. Electron.*, vol. 57, no. 8, pp. 2581–2596, Aug. 2010.

[3] Z. Chen, J. M. Guerrero, and F. Blaabjerg, "A review of the state of the art of power electronics for wind turbines," *IEEE Trans. Power Electron.*, vol. 24, no. 8, pp. 1859–1875, Aug. 2009.

[4] S. Rivera, B. Wu, S. Kouro, V. Yaramasu, and J. Wang, "Electric vehicle charging station using a neutral point clamped converter with bipolar dc bus," *IEEE Trans. Ind. Electron.*, vol. 62, no. 4, pp. 1999–2009, Apr. 2015.

[5] S. Ogasawara and H. Akagi, "Analysis of variation of neutral point potential in neutral-point-clamped voltage source PWM inverters," in *Proc. IEEE Ind. Appl. Soc. Annu. Mtg.*, vol. 2, Toronto, ON, Canada, Oct. 1993, pp. 965–970.

[6] C. Newton and M. Sumner, "Neutral point control for multi-level inverters: theory, design and operational limitations," in *Proc. IEEE Ind. Appl. Soc. Annu. Mtg.*, New Orleans, LA, USA, Oct. 1997, pp. 1336–1343.

[7] N. Celanovic and D. Boroyevich, "A comprehensive study of neutral-point voltage balancing problem in three-level neutral-point-clamped voltage source PWM inverters," *IEEE Trans. Power Electron.*, vol. 15, no. 2, pp. 242–249, Mar. 2000.

[8] K. Yamanaka, A. Hava, H. Kirino, Y. Tanaka, N. Koga, and T. Kume, "A novel neutral point potential stabilization technique using the information of output current polarities and voltage vector," *IEEE Trans. Ind. Appl.*, vol. 38, no. 6, pp. 1572–1580, Nov./Dec. 2002.

[9] P. Karamanakos, E. Liegmann, T. Geyer, and R. Kennel, "Model predictive control of power electronic systems: Methods, results, and challenges," *IEEE Open J. Ind. Appl.*, vol. 1, pp. 95–114, 2020.

[10] R. Vargas, P. Cortes, U. Ammann, J. Rodriguez, and J. Pontt, "Predictive control of a three-phase neutral-point-clamped inverter," *IEEE Trans. Ind. Electron.*, vol. 54, no. 5, pp. 2697–2705, Aug. 2007.

[11] P. Karamanakos and T. Geyer, "Guidelines for the design of finite control set model predictive controllers," *IEEE Trans. Power Electron.*, vol. 35, no. 7, pp. 7434–7450, Jul. 2020.

[12] P. Karamanakos, T. Geyer, and R. Kennel, "On the choice of norm in finite control set model predictive control," *IEEE Trans. Power Electron.*, vol. 33, no. 8, pp. 7105–7117, Sep. 2018.

[13] T. Geyer and D. E. Quevedo, "Multistep finite control set model predictive control for power electronics," *IEEE Trans. Power Electron.*, vol. 29, no. 12, pp. 6836–6846, Dec. 2014.

[14] E. Liegmann, P. Karamanakos, and R. Kennel, "Real-time implementation of long-horizon direct model predictive control on an embedded system," *IEEE Open J. Ind. Appl.*, vol. 3, pp. 1–12, 2022.

[15] E. Liegmann, P. Karamanakos, T. Geyer, T. Mouton, and R. Kennel, "Long-horizon direct model predictive control with active balancing of the neutral point potential," in *Proc. IEEE Int. Symp. Pred. Control of Elect. Drives and Power Electron.*, Pilsen, Czech Republic, Sep. 2017, pp. 89–94.

[16] T. Geyer, "A comparison of control and modulation schemes for medium-voltage drives: Emerging predictive control concepts versus PWM-based schemes," *IEEE Trans. Ind. Appl.*, vol. 47, no. 3, pp. 1380–1389, May/Jun. 2011.

[17] M. Rossi, P. Karamanakos, and F. Castelli-Dezza, "An indirect model predictive control method for grid-connected three-level neutral point clamped converters with LCL filters," *IEEE Trans. Ind. Appl.*, vol. 58, no. 3, pp. 3750–3768, May/Jun. 2022.

[18] S. Vazquez, R. P. Aguilera, P. Acuna, J. Pou, J. I. Leon, L. G. Franquelo, and V. G. Agelidis, "Model predictive control for single-phase NPC converters based on optimal switching sequences," *IEEE Trans. Ind. Electron.*, vol. 63, no. 12, pp. 7533–7541, Dec. 2016.

[19] F. Donoso, A. Mora, R. Cárdenas, A. Angulo, D. Sáez, and M. Rivera, "Finite-set model-predictive control strategies for a 3L-NPC inverter operating with fixed switching frequency," *IEEE Trans. Ind. Electron.*, vol. 65, no. 5, pp. 3954–3965, May 2018.

[20] A. Mora, R. Cárdenas-Dobson, R. P. Aguilera, A. Angulo, F. Donoso, and J. Rodríguez, "Computationally efficient cascaded optimal switching sequence MPC for grid-connected three-level NPC converters," *IEEE Trans. Power Electron.*, vol. 34, no. 12, pp. 12 464–12 475, Dec. 2019.

[21] S. Vazquez, A. Marquez, R. Aguilera, D. Quevedo, J. I. Leon, and L. G. Franquelo, "Predictive optimal switching sequence direct power control for grid-connected power converters," *IEEE Trans. Ind. Electron.*, vol. 62, no. 4, pp. 2010–2020, Apr. 2015.

[22] P. Karamanakos, M. Nahalparvari, and T. Geyer, "Fixed switching frequency direct model predictive control with continuous and discontinuous modulation for grid-tied converters with LCL filters," *IEEE Trans. Control Syst. Technol.*, vol. 29, no. 4, pp. 1503–1518, Jul. 2021.

[23] T. Geyer, *Model predictive control of high power converters and industrial drives*. Hoboken, NJ: Wiley, 2016.

[24] P. Karamanakos, R. Mattila, and T. Geyer, "Fixed switching frequency direct model predictive control based on output current gradients," in *Proc. IEEE Ind. Electron. Conf.*, Washington, D.C., USA, Oct. 2018, pp. 2329–2334.

[25] Q. Yang, P. Karamanakos, W. Tian, X. Gao, X. Li, T. Geyer, and R. Kennel, "Computationally efficient fixed switching frequency direct model predictive control," *IEEE Trans. Power Electron.*, vol. 37, no. 3, pp. 2761–2777, Mar. 2022.

[26] J. Holtz, "The representation of ac machine dynamics by complex signal flow graphs," *IEEE Trans. Ind. Electron.*, vol. 42, no. 3, pp. 263–271, Jun. 1995.

[27] L. Ben-Brahim and A. Kawamura, "Digital control of induction motor current with deadbeat response using predictive state observer," *IEEE Trans. Power Electron.*, vol. 7, no. 3, pp. 551–559, Jul. 1992.

[28] J. Barzilai and J. M. Borwein, "Two-point step size gradient methods," *IMA J. of Num. Anal.*, vol. 8, no. 1, pp. 141–148, Jan. 1988.

[29] Y. Nesterov, *Introductory lectures on convex optimization: A basic course*. Springer Science & Business Media, 2003, vol. 87.

[30] S. Richter, C. N. Jones, and M. Morari, "Real-time input-constrained mpc using fast gradient methods," in *Proc. IEEE Conf. Decis. Control*, Shanghai, China, Dec. 2009, pp. 7387–7393.

[31] G. M. Joksimović, J. Riger, T. M. Wolbank, N. Perić, and M. Vašak, "Stator-current spectrum signature of healthy cage rotor induction machines," *IEEE Trans. Ind. Electron.*, vol. 60, no. 9, pp. 4025–4033, Sep. 2013.

[32] D. G. Holmes and T. A. Lipo, *Pulse Width Modulation for Power Converters: Principles and Practice*. Piscataway, NJ: IEEE Press, 2003.

[33] D. Schröder and J. Böcker, *Elektrische antriebe-regelung von antriebssystemen*. Springer, 2009, vol. 2.

[34] H. du Toit Mouton, "Natural balancing of three-level neutral-point-clamped pwm inverters," *IEEE Trans. Ind. Electron.*, vol. 49, no. 5, pp. 1017–1025, Oct. 2002.
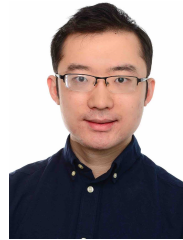
Qifan Yang (S'20) was born in Anhui, China, in 1995. He received the B.Eng. degree in electrical engineering Xi'an Jiaotong University, Xi'an, Shannxi, China, in 2016, and the M.Sc. degree in electrical power engineering from Technical University of Munich, Munich, Germany, in 2019. Since 2019, he has been pursuing the Ph.D. degree at the Chair of Electrical Drive Systems and Power Electronics, Technical University of Munich (TUM), Germany. His research interests include optimal control, power electronics and electrical drives.

Petros Karamanakos (S'10 – M'14 – SM'19) received the Diploma and Ph.D. degrees in electrical and computer engineering from the National Technical University of Athens (NTUA), Athens, Greece, in 2007, and 2013, respectively.

From 2010 to 2011 he was with the ABB Corporate Research Center, Baden-Dättwil, Switzerland, where he worked on model predictive control strategies for medium-voltage drives. From 2013 to 2016 he was a PostDoc Research Associate in the Chair of Electrical Drive Systems and Power Electronics, Technische Universität München, Munich, Germany. Since 2016, he has been with the Faculty of Information Technology and Communication Sciences, Tampere University, Tampere, Finland, where he is currently an Associate Professor. His main research interests lie at the intersection of optimal control, mathematical programming and power electronics, including model predictive control and optimal modulation for utility-scale power converters and ac variable speed drives.

Dr. Karamanakos received the 2014 Third Best Paper Award of the IEEE Transactions on Industry Applications and three Prize Paper Awards at conferences. He serves as an Associate Editor of the IEEE Transactions on Industry Applications and of the IEEE Open Journal of Industry Applications. He is a Regional Distinguished Lecturer of the IEEE Power Electronics Society in the years 2022 and 2023.

Eyke Liegmann (S'16) received the B.Sc. and M.Sc. degrees in electrical power engineering from RWTH Aachen University, Aachen, Germany, in 2013 and 2016, respectively. Currently he is pursuing the Dr.-Ing. degree at the Technical University of Munich, Munich, Germany.

In 2014, he worked as intern at ABB Corporate Research, Västeras, Sweden. From 2015 to 2016, he was with the Institute for Automation of Complex Power Systems—E.ON Energy Research Center—RWTH Aachen University. In 2018, he was visiting Ph.D. student at the Stellenbosch University, Stellenbosch, South Africa. In 2019, he visited Tampere University, Tampere, Finland. His interests are model predictive control of electrical drive systems and the real-time implementation of control algorithms on embedded systems.

Mr. Liegmann received the Best Exhibition Award at the 2016 Power and Energy Student Summit and the 2019 Best Student Paper Award at the 2019 IEEE International Symposium on Predictive Control of Electrical Drives and Power Electronics.
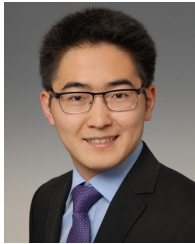
Wei Tian (S'16 - M'22) received the B.Eng. degree in electrical engineering and automation from Central South University (CSU), Changsha, China, in 2012 and the M.Sc. degree in electrical power engineering from RWTH Aachen University, Aachen, Germany, in 2015. Since 2016, he has been pursuing the Ph.D. degree at the Chair of Electrical Drive Systems and Power Electronics, and the Chair of High-Power Converter Systems, Technical University of Munich (TUM), Munich, Germany. His research interests include power electronics and electrical drives, model predictive control, and modular multilevel converter.

Tobias Geyer (M'08 – SM'10 – F'22) received the Dipl.-Ing. degree in electrical engineering, the Ph.D. in control engineering, and the Habilitation degree in power electronics from ETH Zurich in the years 2000, 2005, and 2017, respectively.

After his Ph.D., he spent three years at GE Global Research, Munich, Germany, three years at the University of Auckland, Auckland, New Zealand, and eight years at ABB's Corporate Research Centre, Baden-Dättwil, Switzerland. In 2020, he joined ABB's Medium-Voltage Drive division as R&D platform manager of the ACS6080. In 2022, he became a Corporate Executive Engineer. Working at the intersection of industry and academia he is also an extraordinary Professor at Stellenbosch University, Stellenbosch, South Africa, from the year 2017 until 2023.

He is the author of more than 35 patent families, 150 publications and the book "Model predictive control of high-power converters and industrial drives" (Wiley, 2016). He teaches a regular course on model predictive control at ETH Zurich. His research interests include medium-voltage and low-voltage drives, utility-scale power converters, optimized pulse patterns and model predictive control.

Dr. Geyer received the PELS Modeling and Control Technical Achievement Award in 2022, the Semikron Innovation Award in 2021, and the Nagamori Award in 2021. He also received two Prize Paper Awards of IEEE transactions and two Prize Paper Awards at IEEE conferences. He is a former Associate Editor of the IEEE Transactions on Industry Applications (from 2011 until 2014) and the IEEE Transactions on Power Electronics (from 2013 until 2019). He was an International Program Committee Vice Chair of the IFAC conference on Nonlinear Model Predictive Control in Madison, WI, USA, in 2018. Dr. Geyer is a Distinguished Lecturer of the IEEE Power Electronics Society from the year 2020 until 2023.

Ralph Kennel (M'89-SM'96) was born in Kaiserslautern, Germany, in 1955. He received the Diploma and Dr. Ing. (Ph.D.) degrees in electrical engineering from the University of Kaiserslautern, Kaiserslautern, Germany, in 1979 and 1984, respectively.

From 1983 to 1999, he worked on several positions with Robert BOSCH GmbH (Germany). Until 1997, he was responsible for the development of servo drives. From 1994 to 1999, he was a Visiting Professor with the University of Newcastle-upon-Tyne, Newcastle-upon-Tyne, U.K. From 1999 to 2008, he was a Professor of electrical machines and drives with Wuppertal University, Wuppertal, Germany. Since 2008, he has been a Professor of electrical drive systems and power electronics with Technical University of Munich, Munich, Germany. His current main interests include renewable energy systems, sensorless control of ac drives, predictive control of power electronics, and hardware-in-the-loop systems.

Dr. Kennel is a Fellow of the IEE and a Chartered Engineer in the U.K. within IEEE, he is a Treasurer of the Germany Section as well as ECCE Global Partnership Chair of the Power Electronics society. He is an Associate Editor for the IEEE Transactions on Power Electronics.

Marcelo Lobo Heldwin (S'99-M'08-SM'13) received the B.S. and M.S. degrees in electrical engineering from the Federal University of Santa Catarina (UFSC), Florianópolis, Brazil, in 1997 and 1999, respectively, and his Ph.D. degree from the Swiss Federal Institute of Technology (ETH Zurich), Zurich, Switzerland, in 2007. He is currently the head of the Chair of High-Power Converter Systems with TUM School of Engineering and Design at the Technical University of Munich (TUM), Munich, Germany.

From 1999 to 2003, he worked with industry, including R&D activities at the Power Electronics Institute, Brazil and Emerson Network Power, in Brazil and Sweden. He was a Postdoctoral Fellow at the ETH Zurich and at the UFSC from 2007 to 2009. From 2010 to 2022 he was a Professor with the Department of Electronics and Electrical Engineering at the UFSC. Dr. Heldwein is a member of the Brazilian Power Electronic Society (SOBRAEP) and a member of the Advisory Board of PCIM Europe. His research interests include power electronics, advanced power distribution technologies and electromagnetic compatibility.